Metal Additive Manufacturing

Microstructure and mechanical behaviour of 316L stainless steel produced using sinter-based extrusion additive manufacturing

Ricardo Santamaria[1,*] , Mobin Salasi[1], Sam Bakhtiari[1], Garry Leadbeater[1], Mariano Iannuzzi[1], and Md Zakaria Quadir[1,2]

[1] *Curtin Corrosion Centre, Curtin University, Perth, WA, Australia*
[2] *John de Laeter Centre, Curtin University, Perth, WA, Australia*

ABSTRACT

Specimens were additively manufactured in 316L stainless steel (SS316L) with a technology that combines the extruding method of fused filament fabrication (FFF) with the strengthening stages of metal injection moulding (MIM). A thorough metallographic analysis and tensile testing were carried out to investigate the effect of sintering in the final microstructures, mechanical properties, and fracture modes of the manufactured material. SS316L wrought specimens were also characterised and tested for comparison. Results showed that the sinter-based technology produced a near-fully dense material with a porosity of 1.27% v/v, and a microstructure and mechanical properties comparable to the standard requirements of the UNS S31603 grade. The sintered specimens were characterised at as annealed condition, with fully austenitic microstructures, annealing twins, and sintering defects such as (1) scattered round microporosity, (2) elongated macroporosity, (3) spherical inclusions rich in Si, Mn and O —also found in the precursor powder— and (4) irregular inclusions rich in Cr, Mn and O. The average mechanical properties of the printed SS316L were Young's modulus (E) 196 GPa, 0.2% offset yield strength (Sy) 166 MPa, tensile strength (Su) 524 MPa, elongation after fracture 85% and reduction of area 51%. Based on the findings, a mechanism is outlined explaining the departure from the typical cup-and-cone ductile fracture in the necked region observed in the printed samples.

Introduction

Additive manufacturing (AM), also known as 3D printing, is a general term covering those technologies that allow the fabrication of complex physical objects from digital data by the successive addition of material [1–3]. Regardless of the type of feedstock or binding mechanism, current AM technologies are classified into seven basic categories, i.e. (1) binder jetting, (2) direct energy deposition (DED), (3) material extrusion, (4) material jetting, (5) powder bed fusion (PBF), (6) sheet lamination and (7) vat photopolymerisation [2–4].

SS316L is a widely used stainless steel in the resource sector, due to its favourable corrosion behaviour and good formability. Studies on SS316L fabricated via PBF and DED showed that the manufacturing parameters have a direct impact on the final microstructures, porosity characteristics and mechanical properties [5–15]. Issues with these AM technologies include their initial capital costs, safety concerns in relation to the handling of loose powder and high energy sources, and also, the anisotropic nature of microstructures producing columnar grains [6–8, 15, 16]. Hence, in recent years, investigations have been carried out to address these issues by combining the low cost of extrusion 3D printing techniques using fused filament fabrication (FFF) with the strengthening process of metal injection moulding (MIM). This combined AM technology is referred as metal FFF [3, 17–22].

Manufacturing of SS316L via metal FFF starts with loading the feedstock of pre-alloyed powder embedded in a binder into the 3D printer. The feedstock is then heated just above its binder's melting point, 210 to 290 °C [22–25], allowing it to be extruded line-by-line and layer-by-layer [2–4]. The as-printed object, known as green-part, lacks all the mechanical properties of the final densified metal. To achieve the required strength, the green-part subsequently undergoes a series of post-print processing stages similar to those used in MIM and powder metallurgy (PM) technologies [3, 20, 23, 24]. Solvent debinding is the first stage in metal FFF. Debinding involves removing the primary binder material by dissolving it in a suitable solvent, typically a liquid or gas [13, 24, 26, 27]. The obtained structure, known as brown-part, undergoes the next stage of the process inside a furnace. During this next stage, the remaining secondary binder is burnt off through the porous structures at 425 to 600 °C temperature range, a process known as thermal debinding [21, 23, 25, 27]. The heating rate during thermal debinding is optimised to avoid blistering or cracking of the part. A vacuum atmosphere is used to prevent the oxidation of the steel particles; however, a reducing atmosphere using hydrogen gas can also be employed [24–27]. During the final stage, i.e. sintering, the temperature reaches between 1250 and 1380 °C [23, 25, 26]. During sintering, the specimen is held at this peak temperature for 120 to 180 min [13, 21, 23, 24, 26, 27]. Finally, the sintered part is cooled down to room temperature either inside the furnace or by air quenching [13, 21]. It has been observed that a higher peak temperature and a longer sintering result in microstructures with larger grains and reduced porosity [24, 28, 29].

Recent investigations have reported the microstructure and mechanical properties of FFF fabricated SS316L [13, 17, 18, 21–27, 30–33]. Results show that metal FFF produces porous sintered materials [21, 24, 27], with a relatively large distribution of austenitic grains [13, 24, 27] displaying a ductile behaviour [21, 22] with varying other tensile properties, which are a function of the building orientation [13, 17, 21]. For instance, the porosity varied between < 1% and 16% [17, 26], the average grain size ranged between 25 and 75 μm [13, 17], the yield strength (Sy) varied between 93 and 252 MPa [18, 23], and the tensile strength (Su) ranged between 219 and 561 MPa [18, 30].

The objective of this work was to investigate the relationship between the microstructures, tensile properties and the fracture mechanism of the FFF additively manufactured SS316L. A detailed morphological and microstructural characterisation was carried out using scanning and transmission electron microscopy (SEM and TEM, respectively) and microanalytical techniques, such as electron backscattered diffraction (EBSD) and energy dispersive spectroscopy (EDS). The wrought condition of the SS316L specimens was also tested and analysed, and the results were compared to gain a better understanding of the mechanical and chemical performance of the sintered SS316L material. Results were benchmarked with the literature covering SS316L manufactured by PBF and DED.

Experimental

Manufacturing technology

The SS316L used in this investigation was additively manufactured with a sinter-based extrusion process known as Bound Metal Deposition™ (Desktop Metal®, DM) using the Studio System™ (DM) technology. The system comprises three units, printer, debinder and sintering furnace. The printer uses cartridges containing the feedstock in the form of 6 × 150 mm rods made of pre-alloyed SS316L powder embedded in the wax- and polymer-based binders. The Studio Printer comprises a build volume of 300 × 200 × 200 mm³ and a dual extrusion capability for the ceramic-based media. This media creates an interface between the part and its support structures that is removed after sintering. Once the printing of an object is done, it is moved to the Studio Debinder unit which is an atmospheric pressure, low emission, vapour and odour-tight distillation tank that uses a proprietary solvent solution at 50 °C to remove the wax-based binder and create an open-pore structure. Then, the debound part is moved to the Studio Furnace for sintering. The furnace, which operates under vacuum in an argon-rich atmosphere, eliminates the remaining binder in the brown-part during the heating process and then sinters the part at high temperature, followed by some degree of densification. The entire process is controlled by the cloud-based software Fabricate™ (DM).

Sample manufacture

The dimensions of the SS316L samples for microscopy analysis were 10 × 10 × 3 mm. Subsize tensile specimens were produced per the ASTM E8 recommendations [34], i.e. 100 mm overall length, 6 mm width, 32 mm length in the parallel section, and a 3 mm thickness. All specimens were 3D printed in the XY orientation and Z-direction with the longest dimension laying parallel to the X-axis as shown in schematic Fig. 1a. The extruded line width was 500 μm, the deposited layer height was 150 μm, and the contour shell thickness was 1.5 mm. The top-to-bottom bulk volume was achieved with a linear raster pattern than changed its extruding direction + 45° and −45° with respect to the Y-axis with each deposited layer. The other printing parameters were: extruding temperature 175 °C, extrusion nozzle size

400 μm diameter, extrusion rate 30 mm/s, and build plate temperature 65 °C. The sinter scale factors were $X = 1.16$, $Y = 1.16$ and $Z = 1.15$. This indicates the material allowance of the green-part to compensate for the contractions during the sintering stage. The solvent debinding was conducted for 15 h and the thermal debinding at 550 °C for 2 h. The sintering was performed at a peak temperature of 1350 °C with a dwell time of 2 h. The process ended with furnace-cooling the sintered parts down to room temperature. Figure 1b shows the sintering furnace temperature profile.

Microscopy sample preparation

Feedstock rods (cut longitudinally), brown-part and sintered samples were mounted in cold epoxy resin. Then, they were wet ground from 80 to 1200 grit SiC abrasive paper and then mechanically polished down to a final polish with 0.02 μm alumina suspension. All polished samples were rinsed with ethanol, sonicated in deionized water, dried with nitrogen and placed inside a vacuum desiccator for at least 12 h before the microscopy analysis. Sintered samples for electron backscattered diffraction (EBSD) analysis were additionally ion-milled for 30 min using a beam voltage of 8 kV at a glancing angle of 4° with full cycle rotational movements (TECHNOORG Linda, SEMPrep2). Transmission electron microscopy (TEM) samples were prepared using the focussed ion beam (FIB) lift-out technique on a Dual Beam FIB/SEM instrument (FEI Helios Nanolab G3 CX). The prepared TEM lamella was a strip of 10 × 10 μm² with a thickness below 100 nm. A carbon protective layer was deposited on top of the region of interest using an ion beam with a 30 kV voltage and 0.43 nA current. Trenching, cutting, and thinning steps were carried out at 30 kV and ion beam currents of 9.50–0.23 nA, as the thinning was progressed. After thinning the TEM lamella to a thickness of 100 nm at 30 kV, a final cleaning was applied in two steps: the first step was at a lower voltage of 5 kV for 1 min on each side, followed by a low voltage of 2 kV cleaning for 30 s on either side.

Microstructure investigation

The chemical composition of the powder used in this investigation was verified by quantitative energy-dispersive X-ray spectroscopy (EDS). The analysis
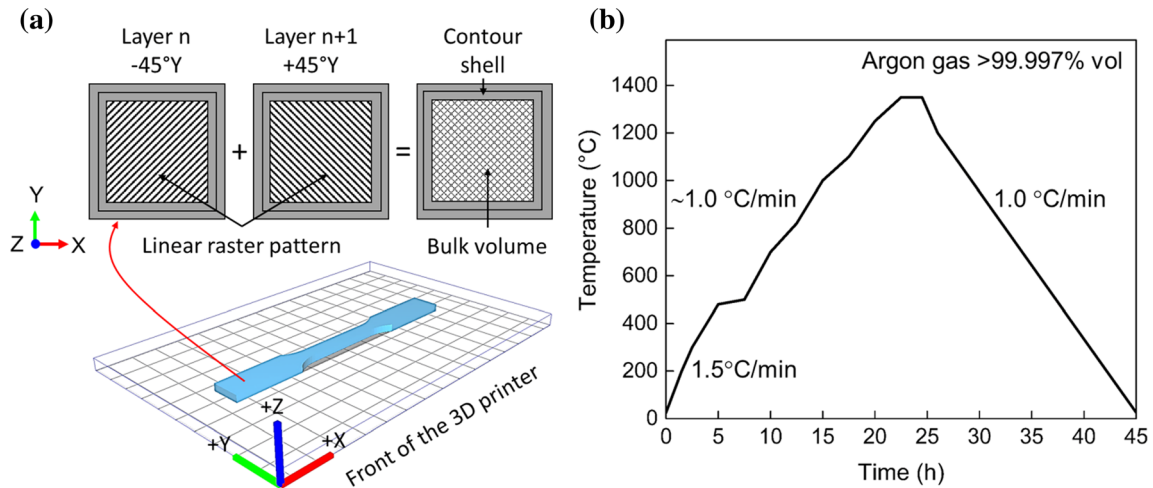
Figure 1 **a** Test specimen 3D printing strategy, and **b** thermal profile used for sintering.

was performed on exposed particles on a section of a brown-part. Measurements were taken with a cobalt calibrated standard using a high sensitivity Oxford EDS detection system coupled to a field emission-scanning electron microscope (FE-SEM) (TESCAN system, CLARA). The quantification was conducted using the Oxford Aztec software. The chemical composition of a SS316L wrought sample was also quantified for comparison. The microstructure of the sintered material was imaged using the SE detector in the FE-SEM, and its chemical composition was mapped using EDS. The microstructure of the SS316L wrought sample was also obtained by FE-SEM for comparison. The particle size of the SS316L powder was measured with the open-source ImageJ software by analysing the FE-SEM images of the feedstock taken at different magnifications using both secondary electron (SE) and backscatter (BS) detectors. Imaging and elemental analysis at nanoscale were conducted on a TEM sample with a Field Emission TEM operating at 200 kV beam voltage (FEI, Talos).

The phases present in the SS316L powder and SS316L sintered material were identified via X-ray diffraction (XRD) analysis using a Cobalt K alpha powder diffractometer radiation source operating at 35 kV 40 mA using a LynxEye detector (Bruker D8 Discover). The XRD data were collected over an angular range of 15° to 135° at a step size of 0.015° and a time interval of 0.7 s. Likewise, a SS316L wrought sample was also analysed in the same analytical conditions for comparison.

The volumetric porosity fraction of the SS316L sintered material was determined with X-ray micro-computed tomography (micro-CT) in a $5 \times 5 \times 3$ mm^3 sample cut from the corner of a square specimen to ensure having part of its contour shell and bulk volume. The analysis was conducted using a 3D X-ray microscope with an exposure energy of 140 kV, during an exposure time of 24 h and at a pixel resolution of 2.2 μm (Zeiss 520 Versa). The fraction area of the samples' porosity was quantified with ImageJ by analysing cross-sectional SEM images at different magnifications. The density of the SS316L sintered material was calculated using the Archimedes principle, as described in ASTM B311 [35].

The crystallographic orientation of the SS316L sintered microstructures was mapped with respect to the build direction (Z) using an Oxford symmetry EBSD detector in the Tescan Clara FE-SEM. The data were acquired at 2 μm step size, 28 kV beam energy, and 21.2 mm working distance. Both EDS and EBSD data acquisition were conducted with Aztec data acquisition software, and the EDS and EBSD data post-processing was undertaken using the Aztec and AztecCrystal software, respectively. A clean-up process was applied to the EBSD data to assimilate any non- or mis-indexed points into the surrounding neighbourhood grains. Less than 10% of the points were modified in the process. The grain boundaries were detected with a threshold misorientation of 10° in conjunction with a minimum of 8 pixel of fractional difference of misorientation variation and a kernel size of 3 by 3. The grain size was measured as the maximum Feret diameter. The average grain aspect ratio was calculated as the fitted ellipse aspect ratio with the Σ3 twins ($< 111 > /60°$) boundaries

excluded. The same analysis was conducted on a SS316L wrought sample for comparison.

Mechanical properties

The mechanical properties (yield and tensile strength) of the sintered SS316L samples were measured by tensile testing on triplicate specimens at room temperature (25 °C). Tests were conducted on rectangular subsize specimens using a 50 kN universal testing machine (UTM, Shimadzu) equipped with 50 kN manual non-shift wedge grips. The UTM crosshead speed was set to 0.48 mm/min within the elastic region, while the displacement was measured using an axial extensometer with a gauge length of 25 mm and a travel range of + 100% (Epsilon Tech Corp). The test was paused once the proportional limit was reached, the extensometer was then removed, and the test was resumed at a UTM crosshead speed of 1.6 mm/min until the specimen fractured. Data were collected at a rate of 10 Hz in the elastic region and 5 Hz in the plastic region. The test was monitored with the Trapezium X software. The tensile test, the dimensions of the specimens, and the method to calculate the 0.2% offset yield strength (Sy), tensile strength (Su), elongation after fracture and reduction of area were conducted as per standard ASTM E8 [34]. The elongation at fracture was calculated from the engineering stress–strain curve. The Young's modulus (E) was approximated using the least-squares method from 25 to 100 MPa using the stress–strain data as recommended in the standard ASTM E111 [36]. All fracture specimens were cut transversely (YZ plane) to a length of 10 mm, sonicated in ethanol, rinsed with deionised water, dried with nitrogen and placed inside a vacuum desiccator for at least 12 h before the microscopy analysis. Fractured surfaces were imaged using the SE detector, and micro-chemical analysis was conducted by EDS. The wrought SS316L specimens used for comparison were wire-cut with the same dimensions from a 3-mm-thick plate and similarly tested and analysed.

Results

Microstructures and analysis

Table 1 presents the chemical composition of SS316L powder and SS316L wrought samples measured by quantitative EDS along with the nominal composition of UNS S31603 as per standard ASTM A240 [37]. From comparisons, the analysed powder metal met the UNS S31603 requirements. A representative FE-SEM image of the feedstock is shown in Fig. 2. The measured average particle size distribution was d50 1.4 μm and d90 5.0 μm. A representative TEM image and corresponding EDS map of the SS316L precursor powder in Fig. 3 show the presence of spherical Si-, Mn- and O-rich inclusions. The inclusion size varies between 0.02 and 0.23 μm.

The XRD spectra of representative SS316L powder and sintered samples measured with respect to its build direction (Z) are shown in Fig. 4. The SS316L wrought data were added for comparison. It can be seen from the figure that the SS316L powder consisted mainly of γ (FCC) austenite phase with a subtle presence of retained δ (BCC) ferrite. According to T. Kurzynowski et al. [6], the retention of δ-ferrite in the powder feedstock results from the rapid solidification of molten SS316L during the gas atomisation process, when the δ-ferrite stabilisers, such as Cr, Mo and Si, segregate to create later localised site-specific metastable conditions in the austenitic matrix [6]. The XRD data of the SS316L sintered sample solely shows γ (FCC) austenitic phase confirming the full dissipation of the δ-ferrite. Wrought data was added for comparison.

Figure 5 shows a large field of view SEM images of the SS316L wrought and sintered samples. The grayscale contrasts indicate the presence of larger austenitic grains in the sintered sample than the wrought sample. Both samples comprise twin boundaries. There is a high porosity and oxide inclusion content in the sintered sample.

The micro-CT reconstruction in Fig. 6 reveals the presence of the elongated defects correlated with the printing raster pattern. The scan from the contour shell shows a cumulative stack of parallel lines as expected from the layer-by-layer print built up. The total scanned volume was 6.9×10^9 μm^3, in which the porosity volume was 8.75×10^7 μm^3, i.e. 1.27% v/v. The total amount of macro- and microporosity were 0.85% and 0.43%, respectively. The threshold

Table 1 Quantitative EDS chemical composition of SS316L powder, SS316L wrought and nominal UNS S31603

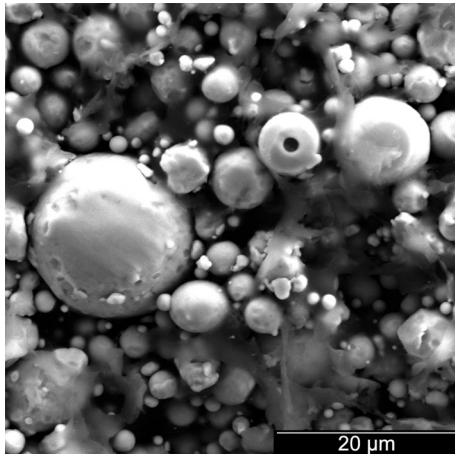| Chemical composition in wt%						
Material	Fe	Cr	Ni	Mo	Mn	Si
SS316L Powder	Bal	17.1	10.0	2.3	1.3	0.6
SS316L Wrought	Bal	17.8	10.0	2.1	1.6	0.5
UNS S31603 [37]	Bal	16–18	10–14	2–3	2 max	0.75 max

Figure 2 FE-SEM image of the feedstock showing the SS316L powder with a particle size distribution of d50 1.4 μm and d90 5.0 μm.
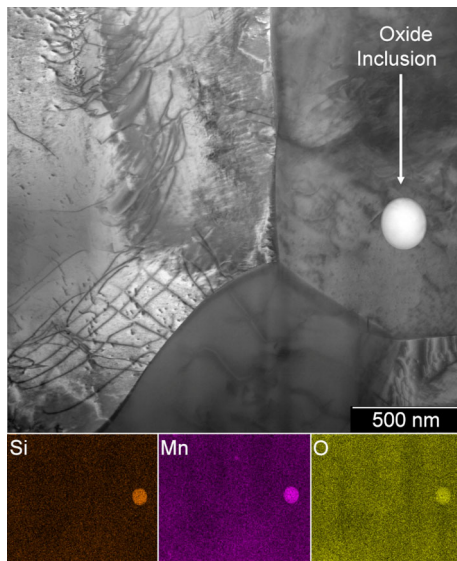

Figure 3 TEM image and corresponding EDS map of a SS316L particle showing a spherical inclusion rich in Si, Mn and O content found in the SS316L precursor powder.

used to define micropores was $< 10{,}000$ μm^3. The fractional area of porosity measured from post-processed SEM cross-sectional images was $4.8\% \pm 1.4$.
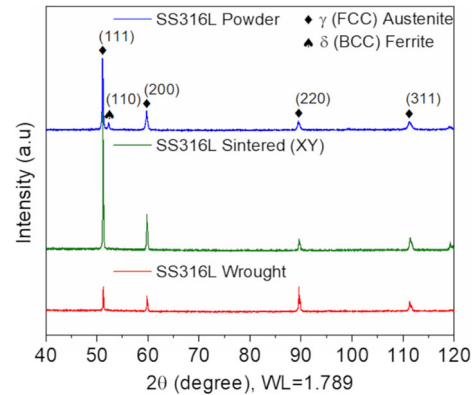

Figure 4 XRD spectra of SS316L powder showing an γ (FCC) austenite phase with a small presence of retained δ (BCC) ferrite (top), SS316L sintered sample (XY plane) showing a fully γ (FCC) austenite phase (middle), and SS316L wrought also showing a fully γ (FCC) (bottom).

The density of the sintered sample obtained using the Archimedes principle was 7.43 g/cm^3 $\pm$ 0.07.

A SEM image of a SS316L sintered sample with corresponding EDS elemental maps is given in Fig. 7. The images show the presence of two types of inclusions, namely (1) irregular Cr-rich particles with an average size of 3 μm and (2) spherical Si-rich particles with an average size of 1.4 μm. Both types contain Mn and O. Identical findings are also reported in other investigations in 3D printed SS316L produced via PBF [38] and DED [12]. According to P. Deng et al. [38], the Si–Mn–O particles in the precursor powder were generated during the gas atomisation process [38]. Yan et al. [39] observed both inclusion types in PBF manufactured SS316L and concluded the particles were Rhodonite (MnSiO$_3$) and Spinel (MnCr$_2$O$_4$) [39]. However, the absence of these phases in the XRD spectra might suggest an amorphous nature of these inclusions, which deserves further investigations.

Figure 8 shows a wide area EBSD map of the Z-cross section (normal to the built direction) of a sintered sample is shown with the corresponding colour-coded inverse pole, indicating a weakly
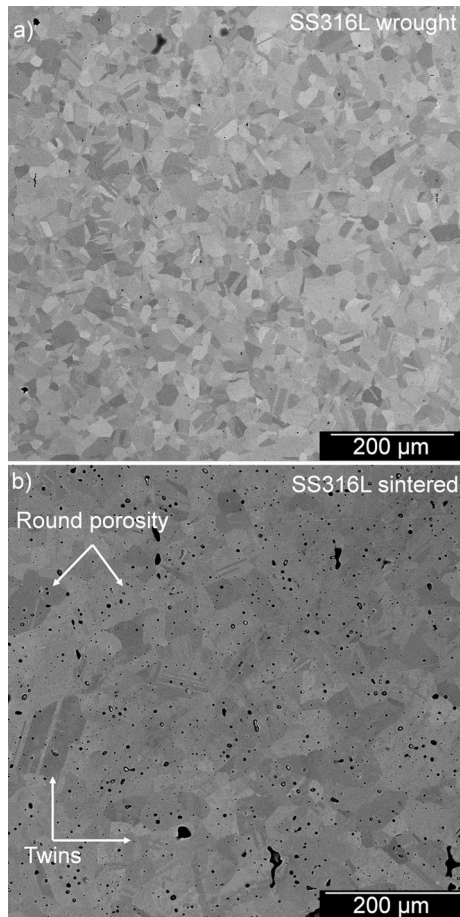
Figure 5 SEM images showing large recrystallised microstructures in the **a** SS316L wrought, and **b** sintered samples, with the later showing distributed porosity, inclusions and twin interfaces.

textured almost random orientation distribution. The almost random orientation is also consistent with the low intensity ($\times$ 1.26 random) in the {111} pole figure. It should be noted that the EBSD area covered is inadequate for the measured grain size, but as a non-textured characteristic was found, it was not regarded as critical. The twin content was measured as the length fraction of the $\Sigma 3$ boundaries in the microstructure, which was 52.3% of $> 10°$ boundaries. This finding is identical to the 53% reported by Irukuvarghula et al. [40] in hot isostatic pressing (HIP) processed SS316L steels [40]. The quantification made from the grain size measurement is shown in Table 2. In comparison, the SS316L wrought sample showed a slight strengthening of the texture as seen in the {111} pole figure, assumed to be caused by the processing history of the sample, the detail of which

is beyond the scope of the manuscript. The grain size measurements are shown in Table 2.

Mechanical properties

Representative engineering stress–strain curves of both SS316L sintered and SS316L wrought samples are shown in Fig. 9, along with the dimensions of the test specimens**.** Results have shown that the sintered specimens performed in a ductile manner, which is represented by an initial linear elastic deformation followed by a non-linear permanent deformation. The calculated average Young's modulus (E, 196 GPa $\pm$ 28) matched with other's measurements, i.e. 202 GPa conducted at 25 °C room temperature [42]. The tensile strength (Su, 524 MPa $\pm$ 1) and elongation at fracture (96% $\pm$ 1) met and exceeded the UNS S31603 standard requirements [37]. The 0.2% offset yield strength (Sy, 166 MPa $\pm$ 2) was slightly ($\sim$ 2%) lower than the minimum required. The mechanical properties are summarised in Table 3.

SEM images of the fractured surface of both SS316L wrought and sintered tensile specimens are presented in Fig. 10. The sintered specimens had a ductile fracture, which was characterised by small inclusions located inside the uniformly distributed spherical dimples. The magnified image at the contour shell and bulk volume shows the presence of elongated macro-porosity. No evidence of secondary central cracks or parabolic dimples, usually found from a shear fracture, was observed in the sintered sample; however, these features were found in the fractured surface of the SS316L wrought specimens. A SEM image and corresponding EDS map from the fractured surface of the SS316L sintered specimen confirming the presence of a Si–Mn–O-rich inclusion inside a spherical dimple can be seen in Fig. 11. Finally, photographs of both SS316L sintered and wrought fractured tensile specimens are given in Fig. 12. While both sintered and wrought sample fractured in a ductile manner, the sintered specimen had a smaller necked region. A typical cup-and-cone characteristic is observed in the wrought specimen.

Discussion

The mechanical properties of the 3D printed SS316L in this work were compared with the literature of SS316L additively manufactured via FFF, PBF and

Figure 6 Micro-CT scans of a SS316L sintered sample showing the presence of elongated macroporosity, **a** as a 3D mesh-like pattern at the bulk volume, **b** as a layer-by-layer pattern at the contour shell, and **c** as a layer-by-layer pattern skewed 45° in the XY plane at the bulk.
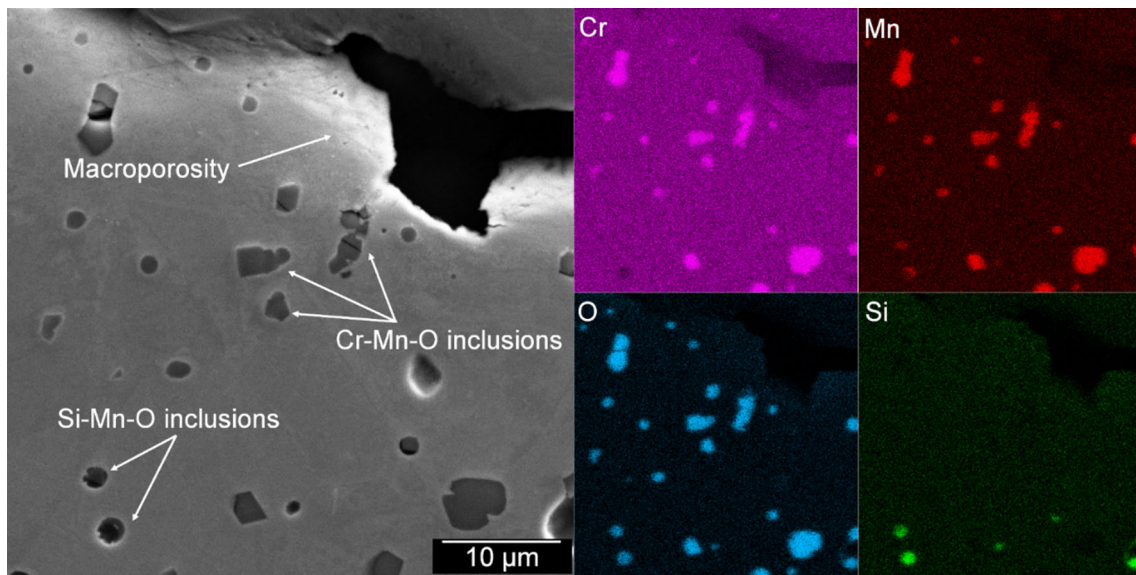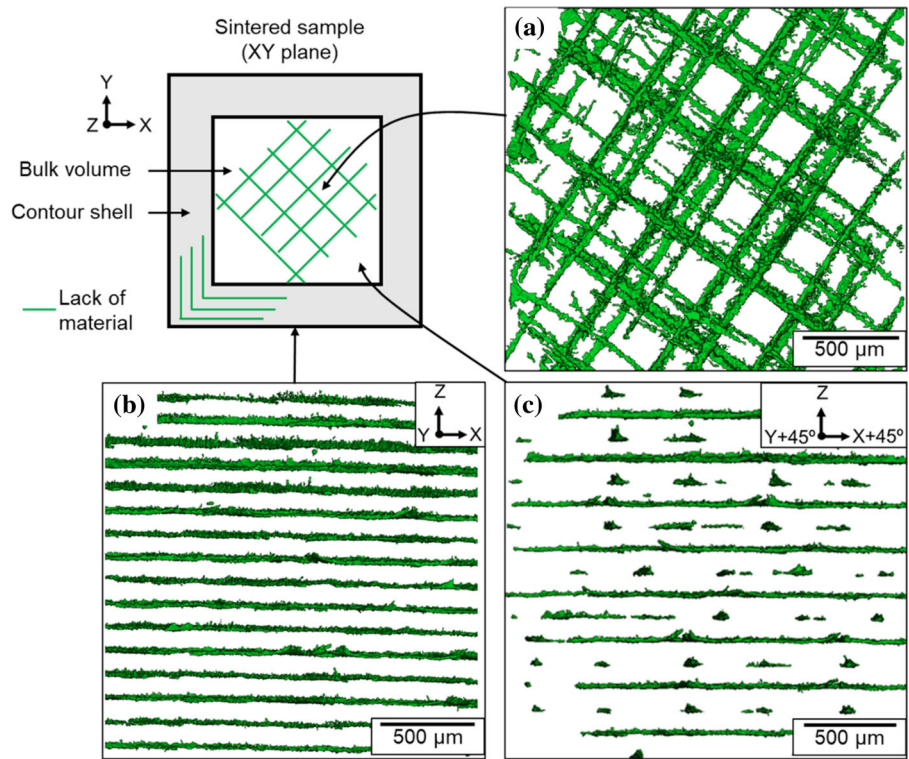

Figure 7 SEM image of a SS316L sintered sample and corresponding EDS elemental maps showing the distribution of Si-Mn–O-rich spherical and Cr-Mn–O-rich irregular inclusions.

DED techniques. The results are summarised in Table 4 which also includes the typical properties obtained from well-established powder-based processes such as MIM and PM. The MIM-316L and UNS standard requirements for the S31603 grade were also added for comparison. Ultimately, some characteristics obtained from the literature such as the size of the precursor powder as well as the average grain size and amount of porosity of the densified SS316L obtained with FFF, PBF and DED processes are given in Table 4 for comparison.
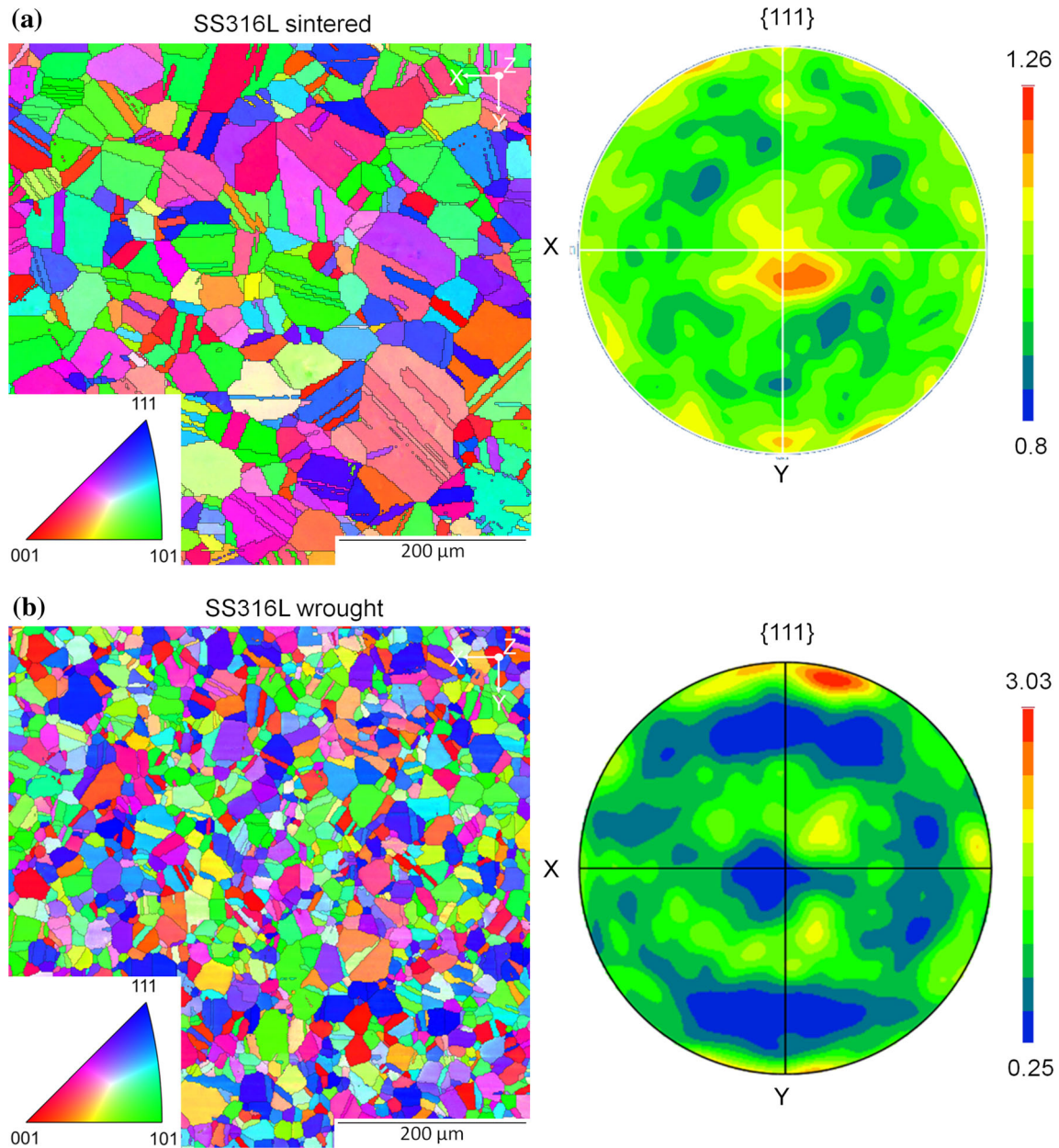
Figure 8 EBSD measured inverse pole figure maps of the **a** SS316L sintered and **b** SS316L wrought sample with corresponding {111} pole figures.

Table 2 Grain size measurements of SS316L sintered and SS316L wrought samples

Material	Overall grain size distribution (μm)	Average grain size (μm)	ASTM grain size No [41]	Average grain aspect ratio
SS316L sintered	d50 35, d90 71	40 ± 23	7.5	3.0 ± 2.4
SS316L wrought	d50 18, d90 34	20 ± 10	9.5	2.3 ± 1.3

Figure 9 Engineering stress–strain curves of both sintered and wrought SS316L materials along with the dimensions of the test specimens.
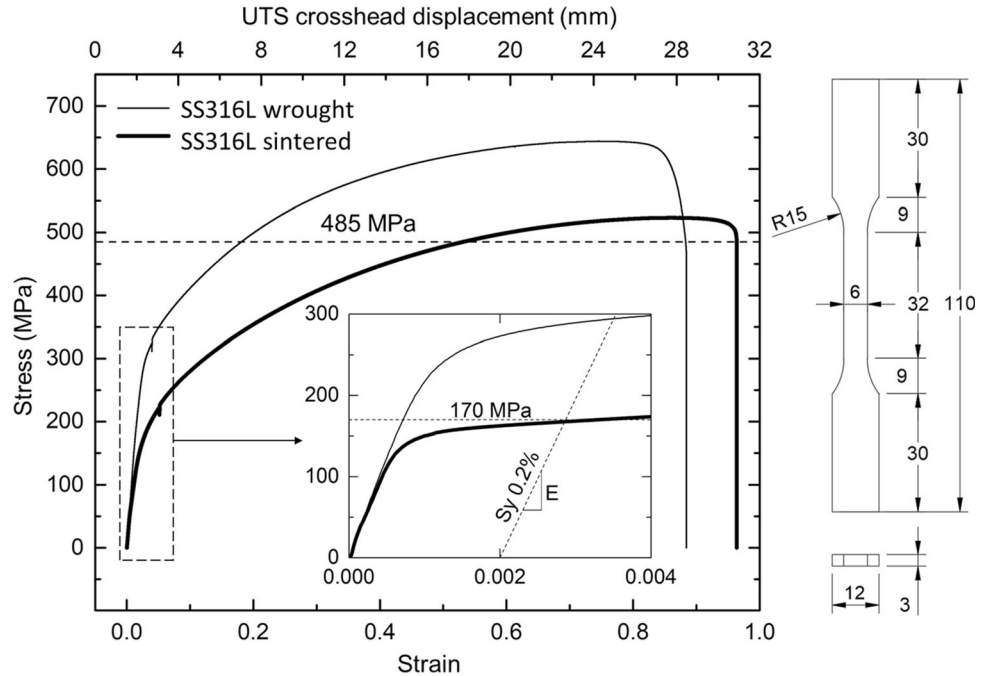

Table 3 Mechanical properties of the SS316L sintered and SS316L wrought samples

Mechanical properties							
Material		Young's modulus (E) (GPa)	Offset Yield strength (Sy) (MPa)	Tensile strength (Su) (MPa)	Elongation at fracture (%)	Elongation after fracture in 32 mm (%)	Reduction of area (%)
SS316L Sintered	Avg	196	166	524	96	85	51
	Min	156	163	523	95	80	50
	Max	216	168	524	96	88	52
	Std Dev	28	2	1	1	3	1
SS316L Wrought	Avg	240	286	644	88	86	55
UNS S31603 [37]		202 [42]	min. 170	min. 485	min. 40	n/a	min. 40

Influence of sintering on the microstructure

This study revealed that the thermal profile in Fig. 1-b for sintering yield an average grain size of 40 μm, which is larger than the observed in the wrought sample. This can be seen in Figs. 5 and 8. The grain growth most likely took place as a result of the high temperature and long dwelling time inside the furnace. Similar grain growth has been reported in other FFF investigations [13, 17, 23]. It is pertinent to note that the grain growth did not led to the formation of a growth-dependent texture. In contrast, due to different thermal processings with the PBF and DED involving a rapid melting followed by a rapid solidification, the produced material is strongly textured, and the microstructure is also asymmetric containing elongated columnar grains in the build direction along with much smaller grains that could grow preferentially along the scanning directions [10, 43].

The micro-CT analysis showed that after sintering, the final porosity of the additively manufactured SS316L was 1.27% v/v, which appears consistent with the findings by Y. Thompson et al. showing less porosity is produced after sintering at higher peak
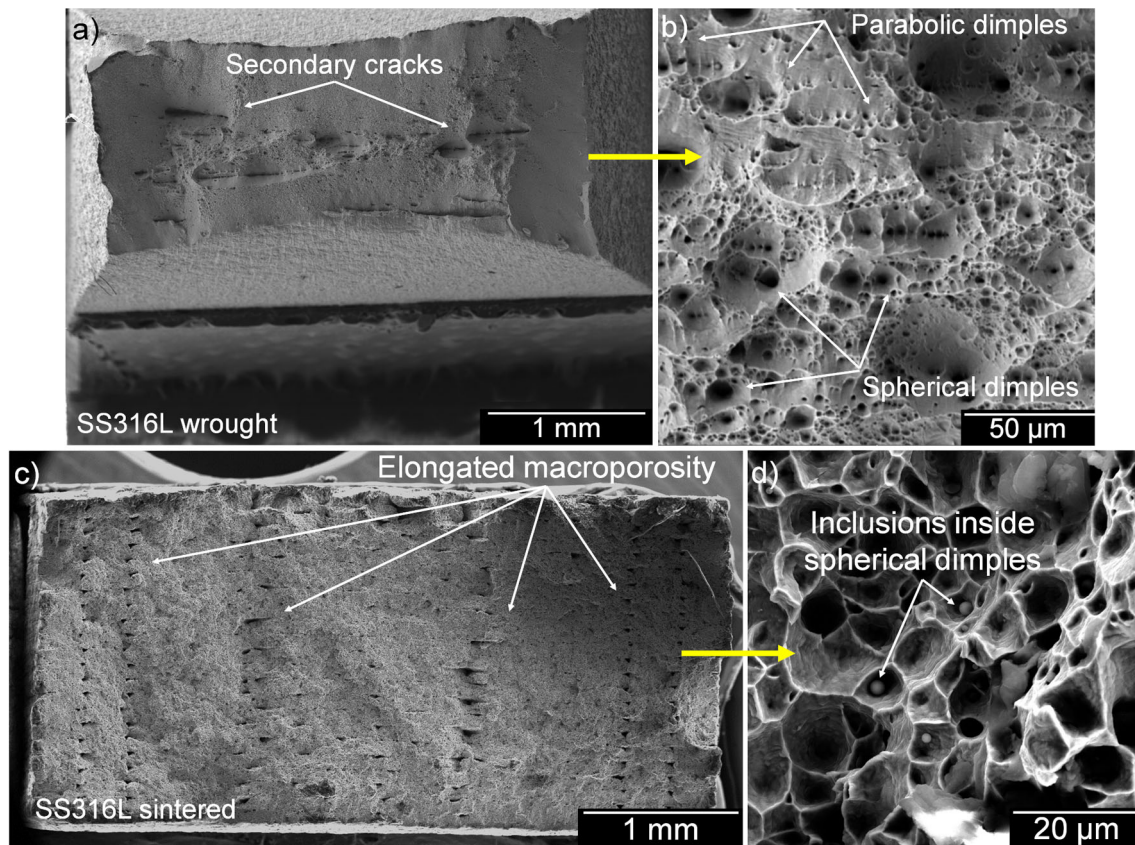
Figure 10 SEM images of the tensile fractured surfaces in the **a** SS316L wrought and **b** sintered specimen showing their microscopy features.
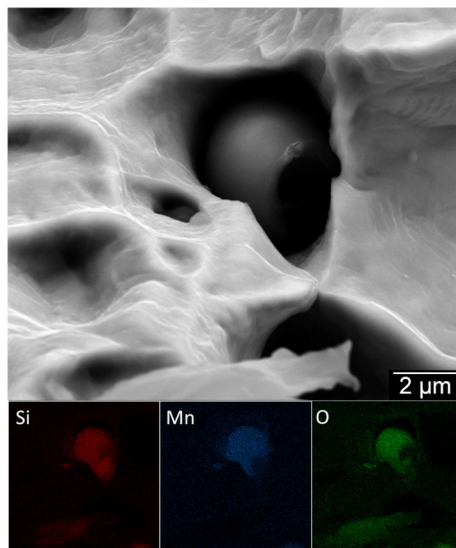

Figure 11 SEM image of a SS316L sintered fractured specimen and corresponding EDS elemental map showing a Si–Mn–O inclusion inside a spherical dimple.

Figure 12 Photographic image of both fractured SS316L sintered tensile specimen (top) and SS316L wrought specimen (bottom) showing two types of necked regions.

printing raster patterns, as it was reported by Damon et al., and Suwanpreecha et al. [17, 19]. Similar effects were also found for PBF and DED [7, 9]. The size of the pre-alloyed powder used for making the feed material used in this investigation was 8 to 30 times smaller than the particles generally used in vast majority investigations with PBF and DED. Therefore, it would be a subject of research how PBF and DED can produce denser objects with a porosity as low as 0.2% [6, 10, 11]. The elongated macroporosity found in the manufactured sintered SS316L is a common defect of the FFF technique due to the inherent nature of the line-by-line and layer-by-layer

temperatures and longer dwell time [24]. The porosity content also depends on the built orientation and

Table 4 Summary of mechanical properties, powder size, grain size and final porosity of SS316L manufactured by Metal FFF, PBF, DED, MIM, PM and standard requirements for UNS S31603 and MIM-316L grade

	Young's modulus (E)	Yield strength (Sy)	Tensile strength (Su)	Elongation at fracture	Powder size	Grain size	Final porosity
Manufacturing technology	(GPa)	(MPa)	(MPa)	(%)	(μm)	(μm)	(%)
S316L sintered (this work)	196	166	524	96	d90 5.0	40 ± 23	1.27
Metal FFF [13]	93−154	168−187	409−499	17−37	n/s	75 ± 20	1.9 − 2.1
Metal FFF [17]	185 ± 5	155−165	500−520	32−37	n/s	25 ± 3	0.5 − 1.7
Metal FFF [18]	n/s	93−105	219−312	6−13	n/s	n/s	4.6
Metal FFF [21]	n/s	n/s	412	56.3	3−15	n/s	7.5
Metal FFF [22]	157.2 ± 4.5	148.0 ± 4.5	443.9 ± 5.9	43.3 ± 2.5	1−10	n/s	9.8
Meta FFF [23]	198	252 ± 7	521 ± 16	9	20−53	45 ± 5	7
Metal FFF [26]	132 ± 65	n/s	296 ± 78	32 ± 16	n/s	n/s	16
Metal FFF [30]	n/s	251	561	53	n/s	n/s	n/s
Metal FFF [31]	n/s	194 ± 19	441 ± 27	29.5 ± 3.8	30−50	n/s	7.8
Metal FFF [32]	152	167	465	31	n/s	n/s	1.5
PBF [6]	219 ± 41	517 ± 38	687 ± 40	32 ± 5	20−63	n/s	< 0.2
PBF [7]	n/s	430−536	509 − 668	12 − 25	20−50	1	1.4−4.8
DED [9]	204 − 218	201 − 284	457 − 509	27 − 42	44 − 106	n/s	< 1.0
DED [10]	n/s	388 ± 42	588 ± 53	48 ± 6	50 − 150	≤ 10	0.1 − 0.2
SS316L Wrought (this work)	240	286	644	88	n/a	20	n/a
PM SS316L [28]	103−144	176−289	308−468	11−19	typ. 12	n/s	12.7−20.6
MIM SS316L [29]	185	180	520	40	n/s	n/s	n/s
UNS S31603 ASTM A240 [37]	202 [42]	min. 170	min. 485	min. 40	n/a	n/a	n/a
MIM-316L ASTM B883 [63]	190	min. 450 typ. 540	min. 450 typ. 520	min. 40 typ. 50	n/s	n/s	n/s

process, regardless of the feedstock or post-processing [2, 44, 45]. This pattern of porosity can be seen in Fig. 6, creating a 3D mesh-like structure inside the bulk volume, and a stack of lines resembling the layer-by-layer printing process in the contour shell of the specimen. The same type of FFF defect is reported elsewhere [17, 19, 21, 22, 27, 33, 46].

Spherical nanosized Si-, Mn- and O-rich inclusions, shown in Fig. 3, were observed in the original feedstock before sintering, which might alter or create a new set of inclusions. Similar findings in the feed powder of additive manufacturing and powder metallurgy processes have been reported elsewhere [28, 38, 39, 47]. Some investigations suggest that these inclusions are formed in the powder during its atomisation process [38, 47]. During sintering, these inclusions may undergo physical and chemical changes and may evolve into a new set of particles, as shown in Fig. 7. The presence of this new type of irregular inclusions rich in Cr, Mn and O, suggests the importance of the sintering process on their morphology. The transformation from the fairly stable Si–Mn–O into the Cr–Mn–O type after the heat treatment of Fe–Cr alloys has also been studied elsewhere [48–51]. These investigations observed that the chemical composition of the Si–Mn–O-type inclusions present in the as-cast Fe–Cr alloys will either remain or change during heat treatment between 1000 and 1300 °C, depending on the initial content of Cr and Si in the steel matrix. Further changes associated with new transformation phenomena—as those occurring post-sintering in the 1100–1200 °C range for the PBF manufactured SS316L alloy—make the matter more complex [51]. The dwell time at peak temperature during the heat treatment

was also found to play important roles for the transformation [48, 51].

Influence of sintering on the mechanical properties

The results presented herein showed that a sinter-based extrusion technology can be used to additively manufacture SS316L with a tensile strength (Su) and ductility in agreement with the standard requirements for the UNS S31603 grade, and a yield strength (Sy) slightly lower ($\sim$ 2%) than the minimum specified [37]. The higher yield strength (Sy) of SS316L wrought, shown in Table 3, can be a contribution of the smaller grain size distribution as per the Hall–Petch equation [52, 53]. However, it should be noted here that many interdependent factors contribute the yield phenomena, and therefore, it should not be further discussed based on the grain size only.

An attempt was made to predict the minimum grain size requirement to attain the UNS S31603 standard benchmark of 170 MPa, assuming the other factors remains constant. The analysis was done using the Hall–Petch parameters experimentally obtained for SS316L wrought alloys in the literature [54, 55]. However, it becomes clear that none of the reported data fit the performance of the sintered material of the present study, i.e. the calculated yield strength (Sy) for a 40 μm grain size was much higher than the 166 MPa obtained herein. The discrepancy of the results with those of the published data could be explained by the fact that there is a significant presence of twin boundaries that were not taken into account in the Hall–Petch calculations. Also, as it is noted earlier, while Hall–Petch provides a great framework for strength prediction, the complexity of the present materials due to the presence of porosity and inclusions makes it difficult to predict and it requires a dedicated approach to simulate.

In order to shed light on the effect of porosity on mechanical properties, it was shown that the PBF and DED processes can produce SS316L with a porosity content that can be as low as 0.2% [6, 10, 11] and hence can exhibit improved yield and tensile strength. Porosity has a detrimental effect on these strength and ductility parameters because of the reduced area supporting the load and the stress concentration factor at each pore [28]. However, an investigation on the effects of sintering conditions on the mechanical properties of MIM SS316L showed

that only the tensile strength and elongation were dependent on the porosity content [56]. Further details on the influence of porosity in the strength of an additively manufactured SS316L via PBF and DED can be seen elsewhere [7, 57].

Regarding ductility, this study indicated that the elongation at fracture of the sintered tensile specimens was in average 70% higher than other metal FFF studies, as shown in Table 4. However, in some of these studies, the reported elongation was not calculated as per the ASTM E8 standard [34], which might explain the difference. When compared to the reported data of PBF and DED manufacturing, the elongation obtained in this study was 20% to 80% higher. The reason might be due to the fact that there is a significant strain field in the PBF and DED manufactured samples that makes a drop in ductility. Some improvements in ductility from the presence of annealing twins have also been reported elsewhere [57–60].

Influence of sintering on the fracture

The SS316L sintered specimens were fractured in a ductile manner. The spherical dimples observed in Fig. 10-d appeared similar in size and uniformly distributed throughout the fractured surface. This mode of fracture is predicted to be caused by the presence of oxide inclusions, as shown in Fig. 7, which acted as the void nucleation sites [52]. The inclusion content, compared to SS316L wrought, is suspected to have led to the voids coalescence into a single crack that lead to the fracture during in tension. As a result, no secondary central cracks nor parabolic dimples were found in the fractography. It is pertinent to note that the presence of parabolic dimples indicates shear fracture [61]. Therefore, the absence of these features in the sintered fracture structure suggests that the material failed in pure tension [61]. The presence of larger voids indicates coalescence in both the wrought and sintered tensile specimens, as shown in Fig. 10b and d, respectively.

Another characteristic observation in the fracture surface of the SS316L sintered specimen was the lack of a cup-and-cone shape at the necked region, as shown in Fig. 12, which is a common feature of a ductile fracture [52, 53]. The reason can be explained by the tensile flow instability phenomena [52]. In short, for a tensile specimen with a rectangular cross section two types of tensile flow instabilities can take

place, i.e. diffuse and localised necking. The transition from diffuse to localised necking, as well as the final extent of each instability mode, depends on the capacity of the material to accommodate strains before the geometrical softening cancels its strain hardening [52]. In other words, when comparing two metals, the one with the higher strain-hardening exponent (n) will tend to maintain the rectangular shape of its cross section for a longer period during the tensile test before the fracture, than the metal with the smaller n-value. The n-value was calculated for both sintered and wrought materials to predict the mode of behaviour by using the tensile test data and following the procedure reported in [52]. The values were 0.56 and 0.44 for the sintered and wrought materials, respectively. It can be seen from the different necked regions in the sintered and wrought specimens in Fig. 12 that the final instability mode was affected by the different n-values. As a result, the sintered specimen showed a larger localised necking than the wrought. Furthermore, when comparing the present investigation results with those from pure copper (99.99%) rectangular tensile specimens, it was found that the instability of the copper specimens was dominated by localised necking, making no cup-and-cone shape [62], because copper has an identical n-value of 0.54 [52].

Conclusions

316L stainless steel was additively manufactured with a sinter-based extrusion technology. A detailed microstructure characterisation, tensile tests, and fractography were conducted to investigate the effects of sintering in the final microstructures and mechanical behaviour of the manufactured materials. Based on the results, the following conclusions can be drawn:

1. The SS316L sintered samples revealed an annealed microstructure composed of fully austenitic grains with an average grain size of 40 μm and 1.27% v/v of combined porosity. Nonemetallic particles, such as Si–Mn–O and Cr–Mn–O inclusions, were also obtained. Nanosized Si–Mn–O-type was found in the SS316L powder, probably as a sub-product of its atomisation process. Further research is required to elucidate the mechanism responsible for the transformation of the Si–Mn–O inclusions into the Cr–Mn–O particles during sintering. Thermodynamic stability studies followed by different stages of sintering and in-depth microstructural analyses using methods, such as TEM-based techniques, will bring new insights into this complex phenomenon.

2. The SS316L sintered samples had a Young's modulus, tensile strength, and ductility comparable to those of a standard UNS S31603 grade; nevertheless, with a yield strength 2% lower than the specified minimum value. The main reason for the lower yield strength was attributed to the relatively large grains as defined by the general Hall–Petch relationship. The detrimental effect of porosity content requires further investigation.

3. The SS316L sintered samples revealed a ductile fracture in pure tension with two distinctive features: i) a fractured surface with uniformly distributed spherical dimples and no secondary cracks, and ii) a necked region without the typical cup-and-cone shape. The first type of fracture surface was proposed to be the product of the larger number of oxide inclusions present in the microstructure compared to the wrought case, leading to the formation of multiple voids coalescing into a single crack. The second fracture surface case was associated with the capacity of the sintered samples to accommodate a larger amount of strain-hardening during the tensile test, compared to the SS316L wrought specimens, which reduced the effect of the diffuse necking while promoting the localised necking instead as the dominating instability mode.

Author contributions

RS: was involved in conceptualisation, methodology, validation, investigation, writing—original draft. MS:

contributed to conceptualisation, supervision, writing—review and editing. SB: was involved in conceptualisation, investigation, data curation. GL: contributed to conceptualisation, writing—review and editing. MI: was involved in writing—review and editing, funding acquisition. MZQ: contributed to supervision, writing—review & editing.

Funding

Declarations

Conflict of interest The authors declare that they have no known competing financial interests or personal relationships that could have appeared to influence the work reported in this paper.

References

[1] ISO/ASTM-52900 (2015) Additive manufacturing — General principles — Terminology. ISO, CH-1211 Geneva 20

[2] Yang L, Hsu K, Baughman B, Godfrey D, Medina F, Menon M, Wiener S (2017) Additive manufacturing of metals: the technology, materials, design and production. Springer, Berlin

[3] Redwood B, Schöffer F, Garret B (2017) The 3D printing handbook: technologies, design and applications. 3D Hubs B.V, Amsterdam

[4] ISO-17296–2 (2015) Additive Manufacturing - General Principles - Part 2: Overview of process categories and feedstock. ISO International, CH-1211 Geneva 20

[5] Rankouhi B, Bertsch KM, Meric de Bellefon G, Thevamaran M, Thoma DJ, Suresh K (2020) Experimental validation and microstructure characterization of topology optimized, additively manufactured SS316L components. Mater Sci Eng, A 776:139050. https://doi.org/10.1016/j.msea.2020.139050

[6] Kurzynowski T, Gruber K, Stopyra W, Kuźnicka B, Chlebus E (2018) Correlation between process parameters, microstructure and properties of 316 L stainless steel processed by selective laser melting. Mater Sci Eng, A 718:64–73. https://doi.org/10.1016/j.msea.2018.01.103

[7] Suryawanshi J, Prashanth KG, Ramamurty U (2017) Mechanical behavior of selective laser melted 316L stainless steel. Mater Sci Eng, A 696:113–121. https://doi.org/10.1016/j.msea.2017.04.058

[8] Casati R, Lemke J, Vedani M (2016) Microstructure and fracture behavior of 316L austenitic stainless steel produced by selective laser melting. J Mater Sci Technol 32(8):738–744. https://doi.org/10.1016/j.jmst.2016.06.016

[9] Kersten S, Praniewicz M, Kurfess T, Saldana C (2020) Build orientation effects on mechanical properties of 316SS components produced by directed energy deposition. Procedia Manuf 48:730–736. https://doi.org/10.1016/j.promfg.2020.05.106

[10] Feenstra DR, Cruz V, Gao X, Molotnikov A, Birbilis N (2020) Effect of build height on the properties of large format stainless steel 316L fabricated via directed energy deposition. Addit Manuf 34:101205. https://doi.org/10.1016/j.addma.2020.101205

[11] Benarji K, Ravi Kumar Y, Jinoop AN, Paul CP, Bindra KS (2021) Effect of heat-treatment on the microstructure, mechanical properties and corrosion behaviour of SS 316 structures built by laser directed energy deposition based additive manufacturing. Met Mater Int 27(3):488–499. https://doi.org/10.1007/s12540-020-00838-y

[12] Aversa A, Saboori A, Librera E, de Chirico M, Biamino S, Lombardi M, Fino P (2020) The role of directed energy deposition atmosphere mode on the microstructure and mechanical properties of 316L samples. Addit Manuf 34:101274. https://doi.org/10.1016/j.addma.2020.101274

[13] Caminero MÁ, Romero A, Chacón JM, Núñez PJ, García-Plaza E, Rodríguez GP (2021) Additive manufacturing of 316L stainless-steel structures using fused filament fabrication technology: mechanical and geometric properties. Rapid Prototyp J 27(3):583–591. https://doi.org/10.1108/RPJ-06-2020-0120

[14] DebRoy T, Wei HL, Zuback JS, Mukherjee T, Elmer JW, Milewski JO, Beese AM, Wilson-Heid A, De A, Zhang W (2018) Additive manufacturing of metallic components – Process, structure and properties. Prog Mater Sci 92:112–224. https://doi.org/10.1016/j.pmatsci.2017.10.001

[15] Yn S, Sun Q, Guo K, Wang X, Liu J, Sun J (2020) Effect of scanning strategies on the microstructure and mechanical behavior of 316L stainless steel fabricated by selective laser melting. Mater Sci Eng, A 793:139879. https://doi.org/10.1016/j.msea.2020.139879

[16] Barkia B, Aubry P, Haghi-Ashtiani P, Auger T, Gosmain L, Schuster F, Maskrot H (2020) On the origin of the high tensile strength and ductility of additively manufactured 316L stainless steel: Multiscale investigation. J Mater Sci Technol 41:209–218. https://doi.org/10.1016/j.jmst.2019.09.017

[17] Damon J, Dietrich S, Gorantla S, Popp U, Okolo B, Schulze V (2019) Process porosity and mechanical performance of fused filament fabricated 316L stainless steel. Rapid

Prototyp J 25(7):1319–1327. https://doi.org/10.1108/RPJ-01-2019-0002

[18] Ait-Mansour I, Kretzschmar N, Chekurov S, Salmi M, Rech J (2020) Design-dependent shrinkage compensation modeling and mechanical property targeting of metal FFF. Prog Addit Manuf 5(1):51–57. https://doi.org/10.1007/s40964-020-00124-8

[19] Suwanpreecha C, Seensattayawong P, Vadhanakovint V, Manonukul A (2021) Influence of specimen layout on 17–4PH (AISI 630) alloys fabricated by low-cost additive manufacturing. Metall Mater Trans A 52(5):1999–2009. https://doi.org/10.1007/s11661-021-06211-x

[20] Poszvek G, Stattler G, Markl E, Seemann R, Lackner M (2021) Fused filament fabrication of metallic components for semi-professional and home use. In: Durakbasa NM, Gençyılmaz MG (eds) Digital conversion on the way to industry. Springer International Publishing, Cham, pp 140–149. https://doi.org/10.1007/978-3-030-62784-3_12

[21] Wang Y, Zhang L, Li X, Yan Z (2021) On hot isostatic pressing sintering of fused filament fabricated 316L stainless steel – Evaluation of microstructure, porosity, and tensile properties. Mater Lett 296:129854. https://doi.org/10.1016/j.matlet.2021.129854

[22] Tosto C, Tirillò J, Sarasini F, Cicala G (2021) Hybrid metal/polymer filaments for fused filament fabrication (FFF) to print metal parts. Appl Sci 11(4):1444. https://doi.org/10.3390/app11041444

[23] Sadaf M, Bragaglia M, Nanni F (2021) A simple route for additive manufacturing of 316L stainless steel via fused filament fabrication. J Manuf Process 67:141–150. https://doi.org/10.1016/j.jmapro.2021.04.055

[24] Thompson Y, Gonzalez-Gutierrez J, Kukla C, Felfer P (2019) Fused filament fabrication, debinding and sintering as a low cost additive manufacturing method of 316L stainless steel. Addit Manuf 30:100861. https://doi.org/10.1016/j.addma.2019.100861

[25] Cerejo F, Gatões D, Vieira MT (2021) Optimization of metallic powder filaments for additive manufacturing extrusion (MEX). Int J Adv Manuf Technol 115(7):2449–2464. https://doi.org/10.1007/s00170-021-07043-0

[26] Rosnitschek T, Seefeldt A, Alber-Laukant B, Neumeyer T, Altstädt V, Tremmel S (2021) Correlations of geometry and infill degree of extrusion additively manufactured 316L stainless steel components. Materials 14(18):5173. https://doi.org/10.3390/ma14185173

[27] Jiang D, Ning F (2021) Additive manufacturing of 316L stainless steel by a printing-debinding-sintering method: effects of microstructure on fatigue property. J Manuf Sci Eng 143(9):091007. https://doi.org/10.1115/1.4050190

[28] German RM (1998) Powder metallurgy of iron and steel. Wiley, 605 Third Ave, New York, NY 10016, USA, 1998. 496

[29] Heaney DF (2012) Handbook of metal injection molding. Woodhead Publishing, Philadelphia, PA

[30] Šafka J, Ackermann M, Machacek J, Seidl M, Véle F, Truxova V (2020) Fabrication process and basic material properties of the basf ultrafuse 316lX material. MM Sci J 2020:4216–4222. https://doi.org/10.17973/MMSJ.2020_12_2020071

[31] Liu B, Wang Y, Lin Z, Zhang T (2020) Creating metal parts by fused deposition modeling and sintering. Mater Lett 263:127252. https://doi.org/10.1016/j.matlet.2019.127252

[32] Gong H, Snelling D, Kardel K, Carrano A (2019) Comparison of stainless steel 316L parts made by FDM- and SLM-Based additive manufacturing processes. JOM 71(3):880–885. https://doi.org/10.1007/s11837-018-3207-3

[33] Gante Lokesha Renukaradhya K (2019) Metal filament 3D printing of SS316L : focusing on the printing process. Student thesis, KTH Royal Institute of Technology, Sweden

[34] ASTM-E8 (2016) Standard test methods for tension testing of metallic materials. ASTM International, West Conshohocken, PA. Doi: https://doi.org/10.1520/E0008_E0008M-16AE01

[35] ASTM-B311 (2017) Standard Test Method for Density of Powder Metallurgy (PM) Materials Containing Less Than Two Percent Porosity. ASTM International, West Conshohocken, PA, 2017. doi: https://doi.org/10.1520/B0311-17

[36] ASTM-E111 (2017) Standard test method for young's modulus, tangent modulus, and chord modulus. ASTM International, West Conshohocken, PA. Doi: https://doi.org/10.1520/E0111-17

[37] ASTM-A240 (2020) Standard specification for chromium and chromium-nickel stainless steel plate sheet and strip for pressure vessels and for general applications. ASTM International, West Conshohocken, PA. Doi: https://doi.org/10.1520/A0240_A0240M-20A

[38] Deng P, Karadge M, Rebak RB, Gupta VK, Prorok BC, Lou X (2020) The origin and formation of oxygen inclusions in austenitic stainless steels manufactured by laser powder bed fusion. Addit Manuf 35:101334. https://doi.org/10.1016/j.addma.2020.101334

[39] Yan F, Xiong W, Faierson E, Olson GB (2018) Characterization of nano-scale oxides in austenitic stainless steel processed by powder bed fusion. Scripta Mater 155:104–108. https://doi.org/10.1016/j.scriptamat.2018.06.011

[40] Irukuvarghula S, Hassanin H, Cayron C, Attallah MM, Stewart D, Preuss M (2017) Evolution of grain boundary network topology in 316L austenitic stainless steel during powder hot isostatic pressing. Acta Mater 133:269–281. https://doi.org/10.1016/j.actamat.2017.04.068

[41] ASTM-E2627 (2019) Standard practice for determining average grain size using electron backscatter diffraction (EBSD) in fully recrystallized polycrystalline materials. ASTM International, West Conshohocken, PA. Doi: https://doi.org/10.1520/E2627-13R19

[42] Ledbetter HM (1981) Stainless-steel elastic constants at low temperatures. J Appl Phys 52(3):1587–1589. https://doi.org/10.1063/1.329644

[43] Pham MS, Dovgyy B, Hooper PA (2017) Twinning induced plasticity in austenitic stainless steel 316L made by additive manufacturing. Mater Sci Eng, A 704:102–111. https://doi.org/10.1016/j.msea.2017.07.082

[44] Colón Quintana JL, Redmann A, Mazzei Capote GA, Pérez-Irizarry A, Bechara A, Osswald TA, Lakes R (2019) Viscoelastic properties of fused filament fabrication parts. Addit Manuf 28:704–710. https://doi.org/10.1016/j.addma.2019.06.003

[45] Montero M, Roundy S, Odell D, Ahn S-H, Wright PK (2001) Material characterization of fused deposition modeling (FDM) ABS by designed experiments. Soc Manuf Eng 10(13552540210441166):1–21

[46] Singh P (2020) Materials-processing relationships for metal fused filament fabrication of Ti-6Al-4V alloy. University of Louisville

[47] Klar E, Samal PK (2007) Powder metallurgy stainless steels: processing, microstructures, and properties. ASM international, Ohio

[48] Shibata H, Kimura K, Tanaka T, Kitamura S-y (2011) Mechanism of change in chemical composition of oxide inclusions in Fe-Cr alloys deoxidized with Mn and Si by heat treatment at 1473 K. ISIJ Int 51(12):1944–1950. https://doi.org/10.2355/isijinternational.51.1944

[49] Shibata H, Tanaka T, Kimura K, Kitamura SY (2010) Composition change in oxide inclusions of stainless steel by heat treatment. Ironmak Steelmak 37(7):522–528. https://doi.org/10.1179/030192310X12700328925903

[50] Ren Y, Zhang L, Pistorius PC (2017) Transformation of oxide inclusions in type 304 stainless steels during heat treatment. Metall and Mater Trans B 48(5):2281–2292. https://doi.org/10.1007/s11663-017-1007-8

[51] Laleh M, Hughes AE, Xu W, Cizek P, Tan MY (2020) Unanticipated drastic decline in pitting corrosion resistance of additively manufactured 316L stainless steel after high-temperature post-processing. Corros Sci 165:108412. https://doi.org/10.1016/j.corsci.2019.108412

[52] Dieter GE, Bacon DJ (1976) Mechanical metallurgy. McGraw-hill, New York

[53] Callister WD, Rethwisch DG, Blicblau A, Bruggeman K, Cortie M, Long J, Hart J, Marceau R, Ryan M, Parvizi R (2021) Materials science and engineering: an introduction. Wiley, Hoboken

[54] Varin R, Kurzydlowski K (1988) The effects of nitrogen content and twin boundaries on the yield strength of various commercial heats of type 316 austenitic stainless steel. Mater Sci Eng, A 101:221–226. https://doi.org/10.1016/0921-5093(88)90068-8

[55] Singh KK, Sangal S, Murty G (2002) Hall-Petch behaviour of 316L austenitic stainless steel at room temperature. Mater Sci Technol 18:165–172. https://doi.org/10.1179/026708301125000384

[56] Yoon TS, Lee YH, Ahn SH, Lee JH, Lee CS (2003) Effects of sintering conditions on the mechanical properties of metal injection molded 316L stainless steel. ISIJ Int 43(1):119–126. https://doi.org/10.2355/isijinternational.43.119

[57] Ronneberg T, Davies CM, Hooper PA (2020) Revealing relationships between porosity, microstructure and mechanical properties of laser powder bed fusion 316L stainless steel through heat treatment. Mater Des 189:108481. https://doi.org/10.1016/j.matdes.2020.108481

[58] Ma S, Fu L, Shan A (2021) Enhancing strength-ductility of the aluminum bronze alloy by generating high-density ultrafine annealing twins. Mater Charact 177:111057. https://doi.org/10.1016/j.matchar.2021.111057

[59] Deng HW, Xie ZM, Zhao BL, Wang YK, Wang MM, Yang JF, Zhang T, Xiong Y, Wang XP, Fang QF, Liu CS (2019) Tailoring mechanical properties of a CoCrNi medium-entropy alloy by controlling nanotwin-HCP lamellae and annealing twins. Mater Sci Eng, A 744:241–246. https://doi.org/10.1016/j.msea.2018.11.143

[60] Kheiri S, Mirzadeh H, Naghizadeh M (2019) Tailoring the microstructure and mechanical properties of AISI 316L austenitic stainless steel via cold rolling and reversion annealing. Mater Sci Eng, A 759:90–96. https://doi.org/10.1016/j.msea.2019.05.028

[61] Mills K, Davis JR (1987) ASM Handbook, Volume 12-Fractography. ASM International,

[62] Ifergane S, Barkay Z, Beeri O, Eliaz N (2010) Study of fracture evolution in copper sheets by in situ tensile test and EBSD analysis. J Mater Sci 45(23):6345–6352. https://doi.org/10.1007/s10853-010-4596-z

[63] ASTM-B883 (2019) Standard specification for metal injection molded (MIM) materials. ASTM International, West Conshohocken, PA. Doi: https://doi.org/10.1520/B0883-19